Scalable Solar-based Adsorption Thermal Battery for Day and Night Heating in Low-carbon Scenario

Ziya Zeng,†[1,2,3] Xinge Yang,†[1,2] Bingchen Zhao,[1,2] Zhihui Chen,[1,2] Kian Jon Ernest Chua,[3] and Ruzhu Wang[1,2,*]

[1]Institute of Refrigeration and Cryogenics, Shanghai Jiao Tong University, Shanghai, 200240, China.

[2]MOE Engineering Research Center of Solar Power and Refrigeration, Shanghai Jiao Tong University, Shanghai, 200240, China.

[3]Department of Mechanical Engineering, National University of Singapore, 9 Engineering Drive 1, Singapore 117576, Singapore.

*Correspondence: rzwang@sjtu.edu.cn

† Equal contribution to this work.

Supplementary Section 1. Optimum design of the ICFB composition ratio

(1) The optimal content of $CaCl_2$ solution

Regarding ICFB sorbent, calcium chloride ($CaCl_2$), which is impregnated into the fiber, functions by capturing moisture and converting it into liquid water. During the sorption process, the ICFB sorbent absorbs moisture and forms various hydrates including $CaCl_2·H_2O$, $CaCl_2·2H_2O$, $CaCl_2·4H_2O$, $CaCl_2·6H_2O$, eventually reaching a $CaCl_2$ solution with stable salt concentration. The sorption performance of ICFB can be optimized by adjusting the salt content. Generally, higher salt content results in better sorption performance and a higher likelihood of liquid leakage occurring. In this case, the salt content should be set as close as possible to the critical deliquescent value. A typical working condition of 20 ^{o}C and 70%RH is used here to determine the optimal $CaCl_2$ content. Once the water vapor sorption reaches equilibrium, the concentration of the $CaCl_2$ solution is ~20 wt.% at 20 ^{o}C and RH70%. By immersing fiber brick into a 20 wt.% $CaCl_2$ solution and subsequently drying it, ICFB exhibits excellent sorption performance. In this study, three ICFB sorbent fabricated using different $CaCl_2$ solutions with a salt content of 15 wt.%, 20 wt.%, and 25 wt.%, were tested to demonstrate the liquid leakage phenomenon.

(2) The optimal content of the carbon nanospheres

Carbon nanospheres determine the photo-thermal behavior of the ICFB sorbent. Experiments to optimize the optimal content of carbon nanospheres in the ICFB sorbent were conducted involving different loadings of carbon particles, from a commercial carbon ink with a solid content of 0.0817 g per 1 ml ink. Five different carbon loadings in the ICFB sorbent, 0.5 wt.%, 2 wt.%, 5 wt.%, 8 wt.%, 12 wt.%, were tested. The influences of carbon content on the solar absorbance, sorption capacity and desorption performance of the ICFB sorbent were investigated in this study. In the sorption experiments, sorbent samples with different carbon loadings that had been completely dehydrated were placed in a constant temperature and humidity chamber, where moisture was adsorbed for 12 hours at 20 ^{o}C and 70%RH. Subsequently, the water-saturated samples were exposed to solar simulator at an intensity of 1 kW m^{-2} for 3-h desorption, with the surface temperature and mass loss of the samples recorded during the desorption process.

Supplementary Section 2. Determination of sorption rate coefficient

In general, the water absorption process of the composite adsorbent can be divided into three stages: i) external diffusion, the gaseous water molecules transport from the free space of air to the external surface of the adsorbent; ii) internal diffusion, the water molecules diffuse in the pores of the composite adsorbent and reach the surface of adsorption sites; and iii) adsorption, water molecules are adsorbed by physical adsorption of SG and chemical adsorption (or absorption) of hygroscopic salt until the adsorption equilibrium is reached, and the water molecules will change from a free state closer to the gas phase to an adsorbed state closer to the liquid phase.

Sorption kinetics reveals the dynamic behaviors of sorption process and indicates the instantaneous adsorption/desorption rates. The linear driving force (LDF) model, established upon the intramolecular transport phenomenon for spherical particles, has been recognized as a well-fitted theoretical method for the assessment of kinetics of the adsorbents in packed-bed reactors. In this model, it is assumed that the all adsorption sites always reach equilibrium at local temperatures and pressures. The LDF model was adopted for the assessment of kinetics of the composite sorbents used in this study, and is defined by the equation:

$$\frac{\mathrm{d}w}{\mathrm{d}t} = K_{\mathrm{LDF}}(w_{\mathrm{eq}}\text{-}w) \tag{1}$$

where t is the relative time (s), K_{LDF} is the coefficient of sorption rate (s^{-1}), which is acquired by fitting the dynamic water uptake curves of the adsorbent. And w_{eq} refers to the equilibrium water uptake of the sorbents (g g^{-1}), determined by the adsorption isotherm as a function of adsorption temperature and vapor pressure. It can be rewritten as the following:

$$\chi = \frac{w\text{-}w_0}{w_{\mathrm{eq}}\text{-}w_0} \tag{2}$$

Where χ is a dimensionless parameter of sorption quantity. After complete dehydration, the initial water uptake, w_0, can be assumed to be zero. Then, the final fitting equation can be obtained as follows:

$$\chi = 1 - \exp(-K_{\mathrm{LDF}}t) \tag{3}$$

Supplementary Section 3. Performance index definitions

To evaluate the heating power performance of the ATB prototype, power density is adopted in this study. It is defined as

$$P = \dot{m}_a \cdot (c_{po} \cdot T_o - c_{pi} \cdot T_i)/V_s \ \ [\text{kW m}^{-3}] \tag{4}$$

where K_{LDF} is the coefficient of sorption rate (s^{-1}) (more details presented in Supplementary Information), and t is the relative time (s). The temperature, humidity and the velocity of the air flow along the reactor are measured during the adsorption/desorption experiments. Heating power and thermal charging/discharging efficiency in all cases are then determined. The thermal energy storage density is thus computed as

$$ESD_t = w \cdot \rho_s \cdot h \ \ [\text{kWh m}^{-3}] \tag{5}$$

where w [g$_{water}$ g$_{adsorbent}^{-1}$] represents the water uptake of the sorbent, ρ_s is the mass density of the adsorbent measured to be 735 kg m^{-3}, and h [kJ kg$_{water}^{-1}$] denotes the sorption enthalpy obtained from the STA tests. The performance of thermal energy storage is highly influenced by the actual stored energy, during the inequilibrium charging/discharging of thermal storage systems. The solar conversion efficiency of sorbent is calculated by

$$\eta_{ce} = \frac{\int \dot{m} \cdot h \, dt}{I \cdot A \cdot t} \times 100 \ \ [\%] \tag{6}$$

where $\dot{m}$ is the mass loss rate of the sample during the desorption process, h [kJ kg$_{water}^{-1}$] denotes the water desorption enthalpy, I is the solar intensity, A is the surface area of the sample, and t is the desorption time. h is assumed as 2400 J g^{-1} in this calculation according to the evaporation enthalpy of water. Desorption efficiency is used to assess the regeneration degree of the adsorbent bed during the heat charging process, which can be written as

$$\eta_{de} = \frac{w_{de}}{w_b} \times 100 \ \ [\%] \tag{7}$$

where w_{de} [g$_{water}$ g$_{adsorbent}^{-1}$] is the desorbed water amount in the heat charging process, and w_b [g$_{water}$ g$_{adsorbent}^{-1}$] represents the total water uptake capacity before desorption. Adsorption efficiency, like wise, is adopted as a measuring index of the water uptake degree of the adsorbent bed during the heat discharging process, defined as

$$\eta_{ad} = \frac{w_{ad}}{w_{de}} \times 100 \ \ [\%] \tag{8}$$

where w_{ad} [g$_{water}$ g$_{adsorbent}^{-1}$] denotes the adsorbed water amount in the heat discharging process. Charging efficiency, which is also termed the heat storage utilization efficiency, is another key indicator to assess the thermal behavior of ATB systems. It is defined as the ratio of the actual stored heat Q_a to the charging energy Q_c (including solar energy or/and electricity input), rewritten as the equation below:

$$\eta_c = \frac{Q_a}{Q_c} = \frac{w_{de} \cdot m_s \cdot h}{Q_c} \times 100 \ [\%] \tag{9}$$

where m_s is the mass of the sorbent. Discharging efficiency, denoting the effective thermal delivery performance of the ATB device, is calculated as the ratio between the discharging thermal energy Q_{out} during heat discharging period and the actual stored heat Q_a:

$$\eta_d = \frac{Q_d}{Q_a} = \frac{\int \dot{m}_a \cdot (c_{po} \cdot T_o - c_{pi} \cdot T_i) dt}{Q_a} \times 100 \ [\%] \tag{10}$$

where $\dot{m}_a$ is the mass flow of air, c_{pi} is the specific heat capacity of inlet air, T_i is the temperature of inlet air, c_{po} is the specific heat capacity of outlet air, T_o is the temperature of outlet air. Energy consumption coefficient η_{ec} is defined to show how much electricity is required to generate 1 kWh of thermal energy storage:

$$\eta_{ec} = \frac{Q_e}{Q_t} \ [\text{kWh}_e \ \text{kWh}_{ts}^{-1}] \tag{11}$$

where Q_e is the electricity input, and Q_t is the amount of thermal energy storage. In this study, energy saving is implemented by promoting the proportion of solar energy in ATB desorption, which is represented by η_{es}:

$$\eta_{es} = \frac{w_{de,s}}{w_{de}} \times 100 \ [\%] \tag{12}$$

where $w_{de,s}$ is the desorbed water amount when using solar heating, and w_{de} is total desorbed water amount based on solar heating and electric heating in each heat charging process. Thermal energy utilization coefficient η_{eu} is an index for evaluating the effectiveness of input energy utilization. It can be calculated as

$$\eta_{eu} = \frac{Q_u}{Q_c} = \frac{Q_s + Q_d}{Q_c} \ [\text{kWh}_t \ \text{kWh}_c^{-1}] \tag{13}$$

where Q_u is the useful thermal supply, comprising the sensible heat of outlet air in the heat charging process Q_s and the discharging thermal energy Q_d during heat discharging period.

Supplementary Section 4. Calculation methods used in the simulation model

In general, the water absorption process of the composite adsorbent can be divided into three stages: i) external diffusion, the gaseous water molecules transport from the free space of air to the external surface of the adsorbent; ii) internal diffusion, the water molecules diffuse in the pores of the composite adsorbent and reach the surface of adsorption sites; and iii) adsorption, water molecules are adsorbed by physical adsorption of SG and chemical adsorption (or absorption) of hygroscopic salt until the adsorption equilibrium is reached, and the water molecules will change from a free state closer to the gas phase to an adsorbed state closer to the liquid phase.

Sorption kinetics reveals the dynamic behaviors of sorption process and indicates the instantaneous adsorption/desorption rates. The linear driving force (LDF) model, established upon the intramolecular transport phenomenon for spherical particles, has been recognized as a well-fitted theoretical method for the assessment of kinetics of the adsorbents in packed-bed reactors. In this model, it is assumed that the all adsorption sites always reach equilibrium at local temperatures and pressures. The LDF model was adopted for the assessment of kinetics of the composite sorbents used in this study, and is defined by the equation:

$$\frac{\mathrm{d}w}{\mathrm{d}t} = K_{\mathrm{LDF}}(w_{\mathrm{eq}} - w) \tag{14}$$

where w is the water uptake of sorbent, w_{eq} is the equilibrium water uptake at a specific working temperature and RH, t is the relative time (s), and K_{LDF} is the coefficient of sorption rate (s^{-1}), which is acquired by fitting the dynamic water uptake curves of the adsorbent. And w_{eq} refers to the equilibrium water uptake of the sorbents (g g^{-1}), determined by the adsorption isotherm as a function of adsorption temperature and vapor pressure. It can be rewritten as the following:

$$\chi = \frac{w - w_0}{w_{\mathrm{eq}} - w_0} \tag{15}$$

Where χ is a dimensionless parameter of sorption quantity, and w_0 is the initial water uptake of sorbent before adsorption. After complete dehydration, the initial water uptake, w_0, can be assumed to be zero. Then, the final fitting equation can be obtained as follows:

$$\chi = 1 - \exp(-K_{\mathrm{LDF}}t) \tag{16}$$

The governing equations of mass transfer and mass balance applied to air channel and packed-bed reactor are expressed as follows:

$$\rho_a \frac{\partial \mathbf{u}}{\partial t} + \rho_a(\mathbf{u} \cdot \nabla)\mathbf{u} - \nabla \cdot \left[-p + \mu\left(\nabla \mathbf{u} + (\nabla \mathbf{u})^T\right) - \frac{2}{3}\mu(\nabla \cdot \mathbf{u}) \right] - \rho_a \mathbf{g} = 0 \tag{17}$$

$$\frac{1}{\varepsilon_b}\rho_a \frac{\partial \mathbf{u}}{\partial t} + \frac{1}{\varepsilon_b}\rho_a(\mathbf{u} \cdot \nabla)\mathbf{u}\frac{1}{\varepsilon_b} - \nabla \cdot \left[-p + \mu\frac{1}{\varepsilon_b}\left(\nabla \mathbf{u} + (\nabla \mathbf{u})^T\right) - \frac{2}{3}\mu\frac{1}{\varepsilon_b}(\nabla \cdot \mathbf{u}) \right] - \rho_a \mathbf{g} = 0 \tag{18}$$

$$\frac{\partial c}{\partial t} + \mathbf{u} \cdot \nabla c + \nabla \cdot \left(-D_{vap}\nabla c\right) = 0 \tag{19}$$

$$\frac{\partial c}{\partial t} + \mathbf{u} \cdot \nabla c + \nabla \cdot \left(-D_{eff} \nabla c\right) + \frac{1}{\varepsilon_b} \rho_s \frac{dw}{dt} = 0 \tag{20}$$

The above equations represent the overall mass balance and water vapor mass balance, respectively. ρ_a, c and ρ_s is the density of air, concentration of water vapor and the density of composite adsorbent, respectively. u is the air velocity, D_{vap} is the diffusion coefficient of water vapor, ε_b is the porosity of the ATB packed-bed reactor, q is the water uptake. Adsorption heat as the reaction enthalpy is generated during the water adsorption process, which is used to heat up the airflow. Equation describes the heat transfer and heat balance in the air channel and packed-bed reactor:

$$\rho_a c_{pa} \frac{\partial T}{\partial t} + \rho_a c_{p,a} \mathbf{u} \cdot \nabla T + \nabla \cdot \left(-k_a \nabla T\right) = 0 \tag{21}$$

$$\rho_{eff} c_{p,eff} \frac{\partial T}{\partial t} + \rho_a c_a \mathbf{u} \cdot \nabla T + \nabla \cdot \left(-k_{eff} \nabla T\right) - \rho_s \frac{dw}{dt} h_{ads} = 0 \tag{22}$$

where ρ_a , $c_{p,a}$, k_a are the density (kg m^{-3}), heat capacity (J kg^{-1} K^{-1}) and thermal conductivity (W m^{-1} K^{-1}) of the air, ρ_{cm} , $c_{p,cm}$, and k_{cm} are the local density (kg m^{-3}), heat capacity (J kg^{-1} K^{-1}) and thermal conductivity (W m^{-1} K^{-1}) of the composite adsorbent, respectively. Q represents the heat released by the composite layer during adsorption process. h_{ads} means the adsorption enthalpy (J mol^{-1}). The terms from left to right on the left side of the equation are the total heat capacity, heat convection, thermal conductivity and the released adsorption heat, respectively.

Supplementary Section 5. Energy evaluation method for the solar ATB wall performance integrated into a building

In general, three primary evaluation methods are predominantly employed to investigate the building energy behaviors [1, 2]: (1) Physics-based modeling approach, referred to as the white box model, which relies on a set of mathematical equations to simulate building operation and analyse energy consumption. The white box modeling approach utilizes genetic software tools like TRNSYS, EnergyPlus, Designbuilder, and CFD, leading to reduced experimental costs after model validation [3]. However, it is noteworthy that the setup of the solar wall and building models is time-consuming, especially during the design stage. (2) Data-driven modeling approach, akin to the black box model, utilizing optimized algorithms to predict and simulate building energy consumption based on existing data. While the black box model is easy to construct and computationally efficient, its reliance on extensive training data results in a prolonged training period and is constrained by a forecasting range determined by its training data [4]. (3) Grey box modeling approach, represented by the resistance and capacitance network model, which establishes a simplified mathematical model to simulate the performance of building energy systems. In this study, a mathematical model without iteration is formulated, offering advantages such as reduced dependence on big data and decreased calculation time while maintaining reasonable precision.

The energy calculation methodology for the solar ATB wall draws on the Trombe wall energy calculation method proposed by UNE-EN ISO 13790 [5] and its correction by Ruiz-Pardo et al. [6]. This method is adopted to assess the energy performance of the solar ATB wall integrated into a building, and to perform a comparative analysis with Trombe wall and conventional wall during the heating season in Shanghai. This method has been demonstrated to be applicable in evaluating the energy behaviors of ventilated Trombe wall in diverse locations with different typical climate characteristics [7]. Distinct from the Trombe wall, the solar ATB wall possesses outstanding heat storage capability attributed to its sorption-desorption thermal effect. Consequently, additional heat charging and discharging parameters are introduced into the solar ATB wall model. Given the comprehensive consideration of an entire building energy system in this study, a calculated parameter for the heat dissipation rate of the building area is incorporated into the calculation model. Key model parameters, encompassing solar irradiation, air conditions, heating power, and heating duration time, are extracted from experimental data.

(1) Trombe wall integrated in a building

The heat gain of the energy building system using Trombe wall derives from the solar radiation transmitting through the transparent solar board and air layer, and then absorbed by the massive wall, and the absorbed heat is transferred to the internal building environment by conduction and convection. The heat gain of the Trombe wall based building system $Q_{\text{Gain, Twall}}$ can be calculated by:

$$Q_{\text{Gain, Twall}} = \begin{cases} I_{\text{w}} A_{\text{w}} \alpha_{\text{sol}} F_{\text{S}} F_{\text{F}} F_{\text{W}} g_{\text{w}} \left[U_{\text{o}}(R_{\text{e}} + R_l) + R_{\text{i}} \dfrac{U_{\text{o}}^2}{U_{\text{i}} U_{\text{e}}} \dfrac{\rho_{\text{a}} C_{p,\text{a}} q_{\text{a}}}{A_{\text{w}}} K_{\text{w}} \omega \right] \cdot t_{\text{d}} \\ 0 \end{cases} \quad \text{[kWh]} \qquad (23)$$

where I_{w} is the solar incident radiation intensity (kW m^{-2}). A_{w} is the area of the Trombe wall (m^2). α_{sol} is solar absorption coefficient of the wall behind the transparent solar board. F_{S}, F_{F}, and F_{W} is the frame reduction factor, the shading reduction factor, and the correction factor for non-scattering glazing, respectively. g_{w} is the total solar energy transmittance of the solar board covering the air layer. t_{d} is the solar radiation hours during daytime. U_{o} is the total thermal transmittance of the Trombe wall (W m^{-2} K^{-1}). R_{e} is the external thermal resistance of the transparent solar board between air layer and external environment (m^2 K W^{-1}). R_{i} is the internal thermal resistance of the wall between air layer and interior environment (m^2 K W^{-1}). R_l is the thermal resistance of the air layer between solar board and the wall (m^2 K W^{-1}). U_{i} is the thermal transmittance of the wall containing the air layer (W m^{-2} K^{-1}). U_{e} is the thermal transmittance of the transparent solar board containing the air layer (W m^{-2} K^{-1}). ρ_{a} is the air density (kg m^{-3}). $C_{p,\text{a}}$ is the specific heat capacity of air (J kg^{-1} K^{-1}). q_{a} is the air flow rate through the air layer (m^3 s^{-1}). K_{w} is the non-dimensional parameter related to the air layer temperature. ω is the ratio of the total solar radiation falling on the heat collection element when the air layer is open during the calculation period, which can be expressed by the following equation:

$$\omega = 0.85[1 - \exp(-1.8 \cdot \gamma_{\text{al}})] \qquad (24)$$

where γ_{al} is the ratio of solar heat gain to heat loss of the air layer.

The heat loss of the energy building system using Trombe wall is caused by the temperature difference between Trombe wall and the external environment, and the heat dissipation from the building itself to the external environment. In this case, the heat loss $Q_{\text{Loss, Twall}}$ obtained from [] needs to be modified as:

$$Q_{\text{Loss, Twall}} = \begin{cases} \left[\left(U_{\text{o}} A_{\text{w}} + \rho_{\text{a}} C_{\text{a}} q_{\text{a}} \dfrac{U_{\text{o}}^2}{U_{\text{i}}^2} K_{\text{w}} \delta \right) \cdot \left(T_i - T_{\text{e,d}} \right) + h_{\text{diss}} \cdot A_{\text{f}} \right] \cdot t_{\text{d}} \\ \left[\left(U_{\text{o}} A_{\text{w}} + \rho_{\text{a}} C_{\text{a}} q_{\text{a}} \dfrac{U_{\text{o}}^2}{U_{\text{i}}^2} K_{\text{w}} \delta \right) \cdot \left(T_i - T_{\text{e,n}} \right) + h_{\text{diss}} \cdot A_{\text{f}} \right] \cdot t_{\text{n}} \end{cases} \quad \text{[kWh]} \qquad (25)$$

where δ is the ratio of the accumulated internal-external temperature difference when the ventilation is on, to its value over the whole calculation period. The value of δ is obtained by Eq. (26). $T_{\text{e,d}}$ and $T_{\text{e,n}}$ is the external environment temperature (K) during daytime and nighttime, respectively. T_i is the internal environment temperature (K). h_{diss} is the heat dissipation rate from the building itself to the external environment per building floor area (W m^{-2}). A_{f} is the building floor area (m^2). t_{d} and t_{n} is the heating hours (h) during daytime and nighttime, respectively.

$$\delta = 0.08 \cdot \ln(\gamma_{\text{al}}) + 0.2 \qquad (26)$$

The heating load of the building system using Trombe wall $Q_{\text{total, Twall}}$ is obtained as:

$$Q_{\text{total, Twall}} = Q_{\text{Gain, Twall}} - Q_{\text{Loss, Twall}} \quad \text{[kWh]} \qquad (27)$$

(2) Conventional wall in a building

The conventional wall, which has nether solar energy harvesting behavior nor heat storage capability, is also investigated as a comparison to show the energy saving performance of solar ATB wall. Similar to the energy calculation method of the Trombe wall integrated building system, the heat loss through the building system using conventional wall $Q_{\mathrm{Loss,\,Cwall}}$ is calculated as:

$$Q_{\mathrm{Loss,\,Cwall}} = \begin{cases} \left[\varepsilon U_{\mathrm{c}} A_{\mathrm{c}} \cdot (T_i - T_{\mathrm{e,d}}) + h_{\mathrm{diss}} \cdot A_{\mathrm{f}}\right] \cdot t_{\mathrm{d}} \\ \left[\varepsilon U_{\mathrm{c}} A_{\mathrm{c}} \cdot (T_i - T_{\mathrm{e,n}}) + h_{\mathrm{diss}} \cdot A_{\mathrm{f}}\right] \cdot t_{\mathrm{n}} \end{cases} \text{[kWh]} \qquad (28)$$

where ε is the correction factor for the overall heat transfer coefficient of the opaque conventional building envelope. A_{c} is the area of the conventional wall (m²), which is the same as the area of the Trombe wall. U_{c} is the total thermal transmittance of the conventional wall (W m⁻² K⁻¹). The heating load of the building system using conventional wall $Q_{\mathrm{total,\,Cwall}}$ is obtained as:

$$Q_{\mathrm{total,\,Cwall}} = - Q_{\mathrm{Loss,\,Cwall}} \text{ [kWh]} \qquad (29)$$

(3) Solar ATB wall integrated into a building

The heat gain of the energy building system using solar ATB wall is much complicated involving heat absorption, heat storage, heat release of the ATB wall, which are usually time-varying processes with their mathematical characteristics hard to obtain. To simplify the calculation model, on the basis of the Trombe wall model, an averaged heat charging rate h_{char} (kW m⁻³) is used to describe the heat storage process at daytime, and an averaged heat discharging rate h_{disc} (kW m⁻³) is selected to describe the heat release process at nighttime. The heat gain of the solar ATB wall based building system $Q_{\mathrm{Gain,\,ATBwall}}$ (kWh) can be calculated by:

$$Q_{\mathrm{Gain,\,ATBwall}} = \begin{cases} \left\{ I_{\mathrm{w}} A_{\mathrm{w}} \alpha_{\mathrm{sol}} F_{\mathrm{S}} F_{\mathrm{F}} F_{\mathrm{W}} g_{\mathrm{w}} \left[U_{\mathrm{o}}(R_{\mathrm{e}} + R_l) + R_{\mathrm{i}} \frac{U_{\mathrm{o}}^2}{U_{\mathrm{i}} U_{\mathrm{e}}} \frac{\rho_{\mathrm{a}} C_{\mathrm{p,a}} q_{\mathrm{a}}}{A_{\mathrm{w}}} \mathrm{K_w} \omega \right] - h_{\mathrm{char}} \cdot V_{\mathrm{ATB}} \right\} \cdot t_{\mathrm{d}} \\ h_{\mathrm{disc}} \cdot V_{\mathrm{ATB}} \cdot t_{\mathrm{n}} \end{cases} \qquad (30)$$

where V_{ATB} is the volume of the ATB wall (m³). The values of h_{char} and h_{disc} can be obtained from the experimental data in this study. The heat loss of the energy building system using solar ATB wall is caused by the temperature difference between the wall and the external environment, and the heat dissipation from the building itself to the external environment, which can also be obtained as:

$$Q_{\mathrm{Loss,\,ATBwall}} = \begin{cases} \left[\left(U_{\mathrm{o}} A_{\mathrm{w}} + \rho_{\mathrm{a}} C_{\mathrm{a}} q_{\mathrm{a}} \frac{U_{\mathrm{o}}^2}{U_{\mathrm{i}}^2} \mathrm{K_w} \delta \right) \cdot (T_i - T_{\mathrm{e,d}}) + h_{\mathrm{diss}} \cdot A_{\mathrm{f}} \right] \cdot t_{\mathrm{d}} \\ \left[\left(U_{\mathrm{o}} A_{\mathrm{w}} + \rho_{\mathrm{a}} C_{\mathrm{a}} q_{\mathrm{a}} \frac{U_{\mathrm{o}}^2}{U_{\mathrm{i}}^2} \mathrm{K_w} \delta \right) \cdot (T_i - T_{\mathrm{e,n}}) + h_{\mathrm{diss}} \cdot A_{\mathrm{f}} \right] \cdot t_{\mathrm{n}} \end{cases} \text{[kWh]} \qquad (31)$$

The heating load of the building system using the solar ATB wall $Q_{\mathrm{total,\,ATBwall}}$ is obtained as:

$$Q_{\mathrm{total,\,ATBwall}} = Q_{\mathrm{Gain,\,ATBwall}} - Q_{\mathrm{Loss,\,ATBwall}} \text{ [kWh]} \qquad (32)$$

The accumulated energy saving per unit solar ATB wall compared with conventional wall Q_{ES} is obtained as:

$$Q_{ES} = \frac{Q_{\text{total, ATBwall}} - Q_{\text{total, Cwall}}}{A_w} \quad [\text{kWh m}^{-2}] \tag{33}$$

For the case study evaluating the energy performance of the solar ATB wall integrated into a residential building, the solar ATB wall, with a dimension of 3 m in height and 6 m in width, is installed on the south wall of two bedrooms in the building. The transparent solar board has a heat transfer coefficient of 3.8 W m^{-2} K^{-1}. The convective heat transfer coefficients on the outer surface and inner surface are 23 W m^{-2} K^{-1} and 8.7 W m^{-2} K^{-1}, respectively. The convective heat transfer coefficient in the air layer is 2.5 W m^{-2} K^{-1}, and the radiative surface heat transfer coefficient in the air layer is 4.2 W m^{-2} K^{-1}.

Supplementary Section 6. Results and Discussions
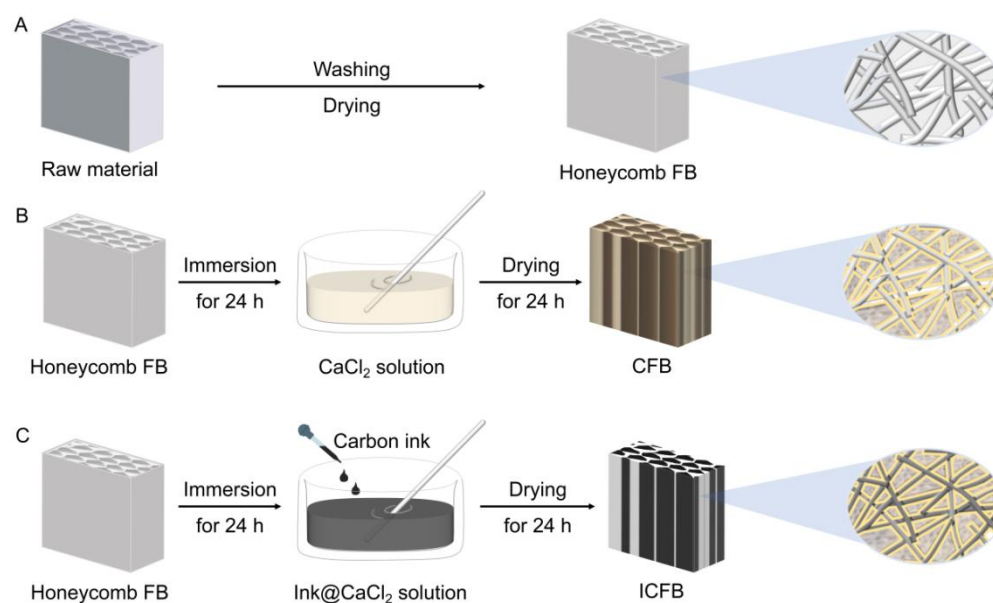
Supplementary Fig. 1. The synthesis processes of (A) FB, (B) CFB, and (C) ICFB. The CFB is prepared by immersing the FB into the 20% wt.% $CaCl_2$ solution for 24 h, and then the obtained composite is dried under 120 °C for 24 h to desorb water. The difference in the preparation of ICFB is to immerse the FB into the 20% wt.% $CaCl_2$ solution mixed with the added carbon ink.
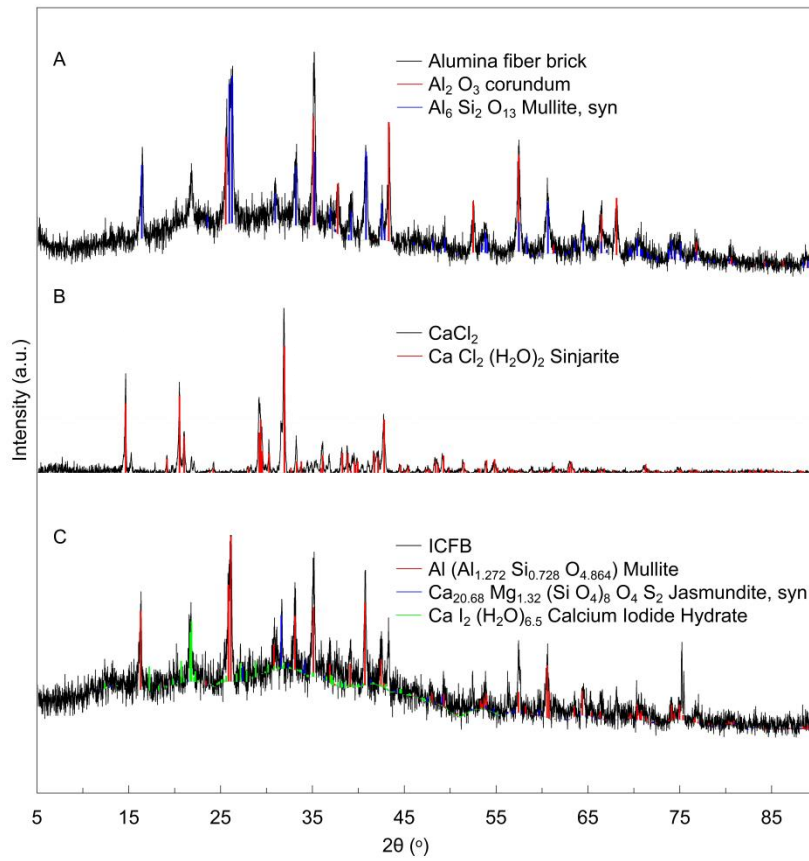
Supplementary Fig. 2. XRD patterns of three samples: (A) FB; (B) CaCl₂; (C) ICFB.
The results of ICFB indicate the successful embedment of $CaCl_2$ crystals into the pores of FB.
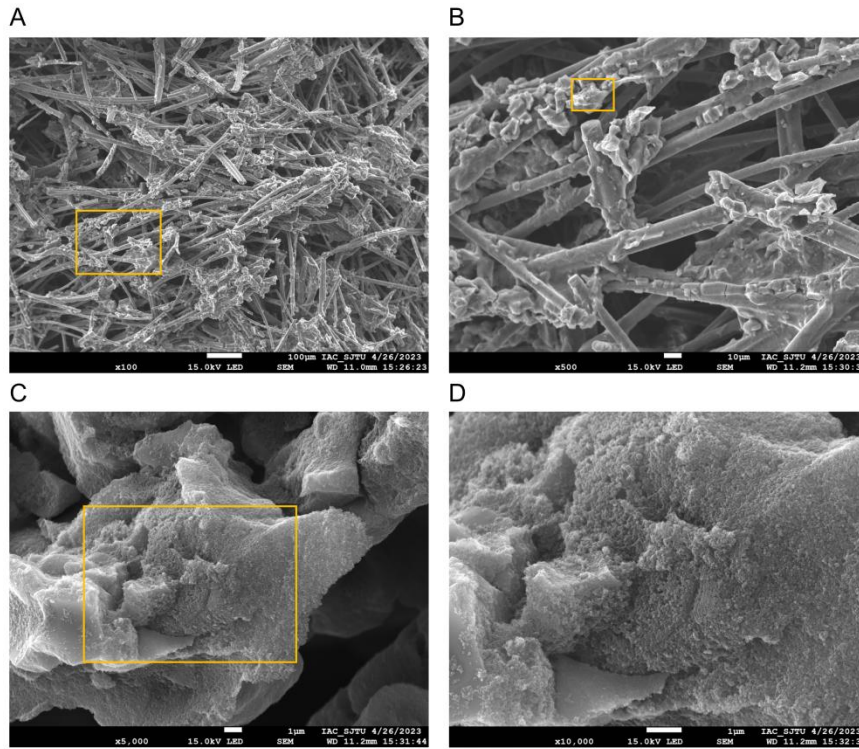
Supplementary Fig. 3. SEM images of CFB under different scale bars: (A) 100 μm; (B) 10 μm; (C) 5 μm; (D) 1 μm. These images are taken by sequentially enlarging the local area of the CFB sample. For example, Figure 2b is the partial image framed in yellow in Figure 2a. The results show the intertwined fabrication of observed fibers and the formation of abundant pores, and the distribution of $CaCl_2$ crystals onto the surface of fibers.
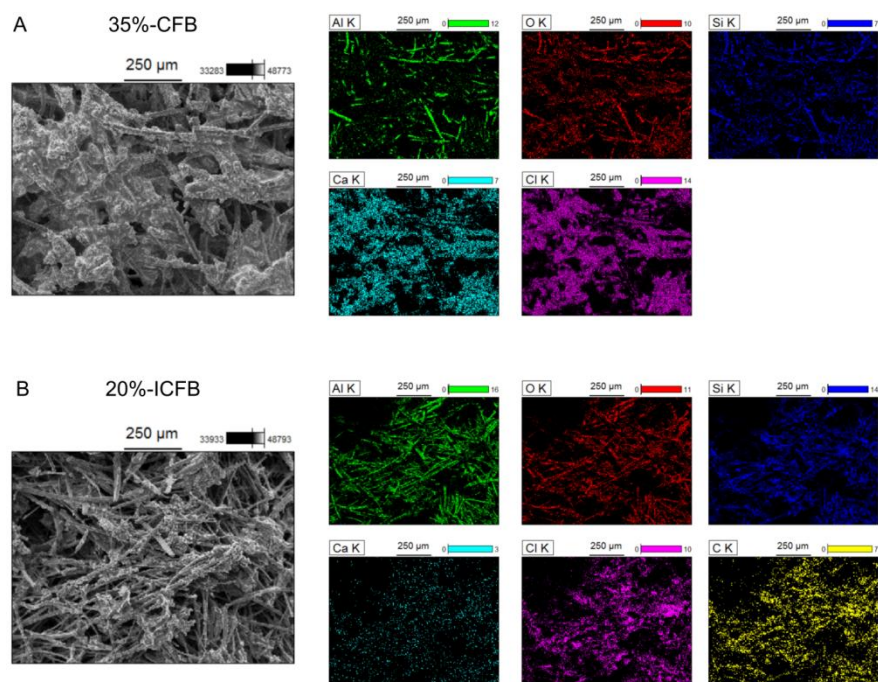
Supplementary Fig. 4. SEM and EDS images of (A) 35%-CFB, and (B) 20%-ICFB.
35%-CFB is fabricated by immersing FB into the 35 wt.% $CaCl_2$ solution, and 20%-CFB is prepared by immersing FB into the 20 wt.% ink@$CaCl_2$ solution. A higher $CaCl_2$ content and the phenomenon of salt agglomeration are observed for 35%-CFB with a larger salt loading. The results also indicate the uniform distribution of $CaCl_2$ and carbon particles in ICFB.

A (15 wt.% CaCl$_2$ solution)
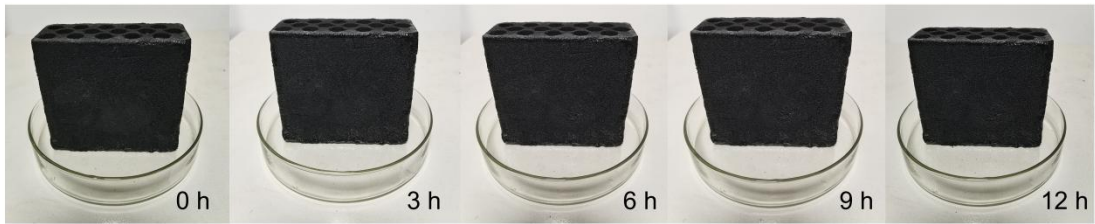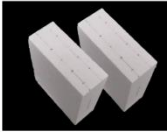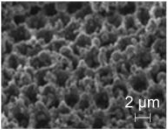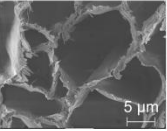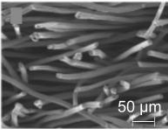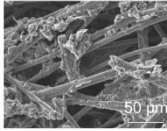
B (20 wt.% CaCl$_2$ solution)
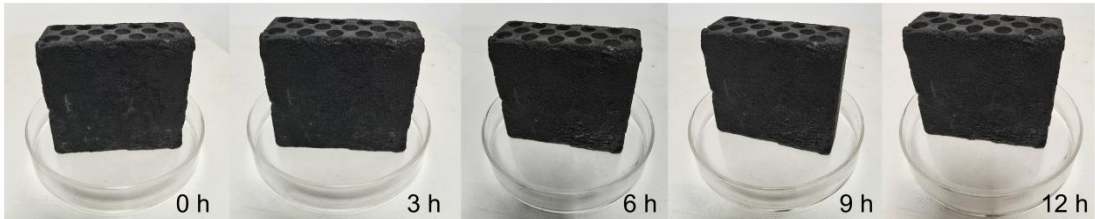
C (25 wt.% CaCl$_2$ solution)
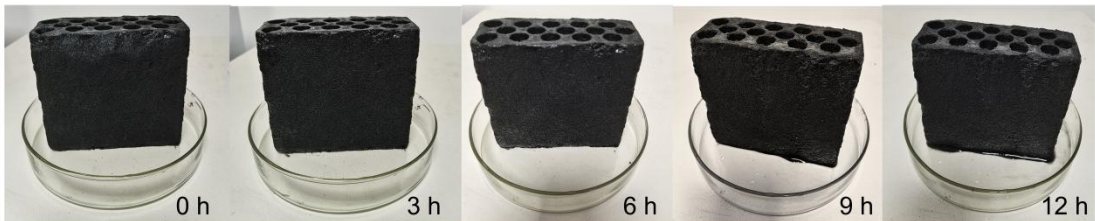
Supplementary Fig. 5. Liquid leakage test of (A) 15%-ICFB, (B) 20%-ICFB, and (C) 25%-ICFB under a 12-h water sorption period. Herein, 15%-ICFB, 20%-ICFB, and 25%-ICFB is fabricated by immersing FB into the 15 wt.%, 20 wt.%, and 25 wt.% CaCl$_2$ solution, respectively. The leakage test is carried out at constant 20 °C and 70%RH for a 12-h sorption period. According to the results, there is no leakage phenomenon observed in the experiments of 15%-ICFB and 20%-ICFB, while distinguished liquid leakage from the 25%-ICFB module is observed on the dish after 9 h. After the liquid leakage test, the ICFB samples are dried and weighted mass. The results show that, the mass change of the 15%-ICFB and 20%-ICFB is negligible, while 25%-ICFB has a 6.4% decrease in mass after 12-h water sorption. To ensure a large heat storage capacity of the ICFB module as well as preventing the leakage problem, 20%-ICFB is selected as optimum.

	A	B	C	D
Sorbent material				
Microscopic characterization				
Porosity (%)	60	70	90	80
Pore volume ($cm^3 g^{-1}$)	0.309	3.97	4.76	1.93
Mass density ($kg m^{-3}$)	2150	70	106	580
Salt loading (%)	22.4	70	90	36
Energy density ($kWh m^{-3}$)	24.7	32.7	127	86.4

Supplementary Fig. 6. Characteristics and performance comparison of four cost-effective sorbent materials in low-humidity scenarios: (A) WSS-22.4 wt.%CaCl$_2$ based on mesoporous siliceous shale (reprinted with permissions from Copyright 2015 Elsevier) [8]; (B) ILCA based on natural loofah (reprinted with permissions from Copyright 2021 Elsevier) [9]; (C) 90wt.%LiCl-SHC based on active carbon fiber (reprinted with permissions from Copyright 2022 Springer Nature) [10]; (D) ICFB in this work. Based on the results, an energy density of 86.4 kWh m^{-3} is obtained for ICFB operating at 20 $^{\circ}$C and 40%RH.
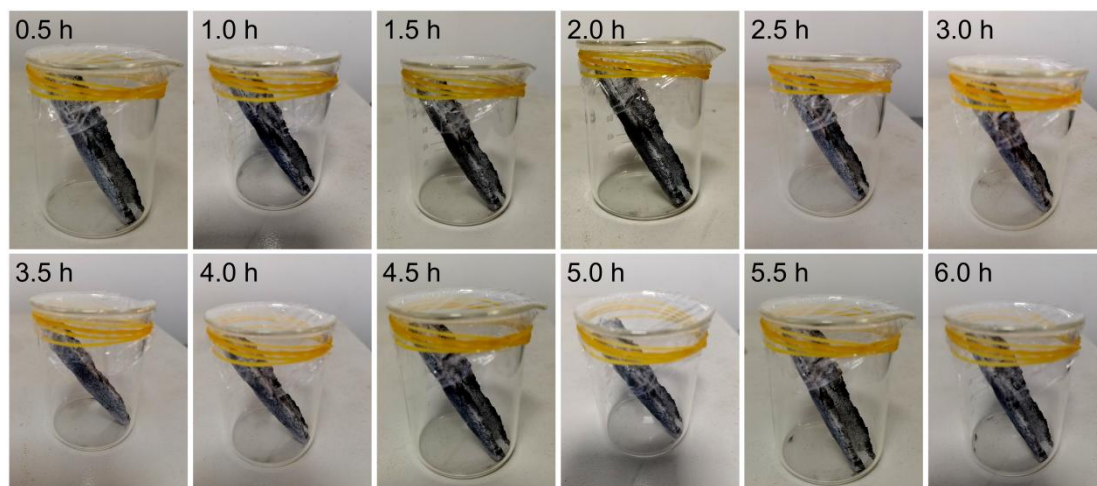
Supplementary Fig. 7. Attachment ability test of the ICFB sample during a shaky condition. The ICFB sample with 5.85 g is placed in a glass beaker, and is put into an 80-W ultrasonic cleaner for a continuous shaky vibration for 6 h. The beaker containing the sample is taken out to observe the detachment phenomenon and weighed every 0.5 h. It is observed that a small amount of powder dropped onto the bottom of the glass after the 6-h vibration.
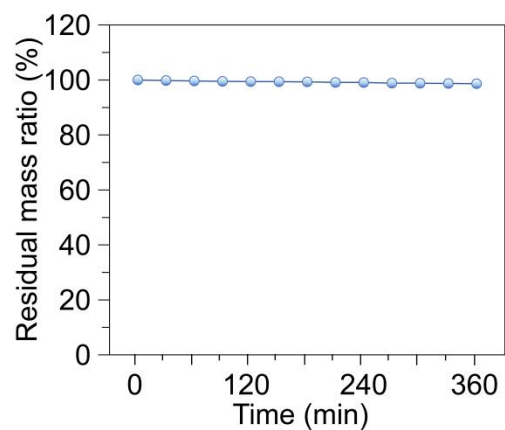
Supplementary Fig. 8. Mass changes of the ICFB sample during the shaky condition simulated by an 80-W ultrasonic cleaner. According to the result, the ICFB sample with 5.85 g has subtle change in residual mass (less than 1.4%) after the 6-h vibration, indicating the strong attachment ability of $CaCl_2$ and carbon particles on the carrier.
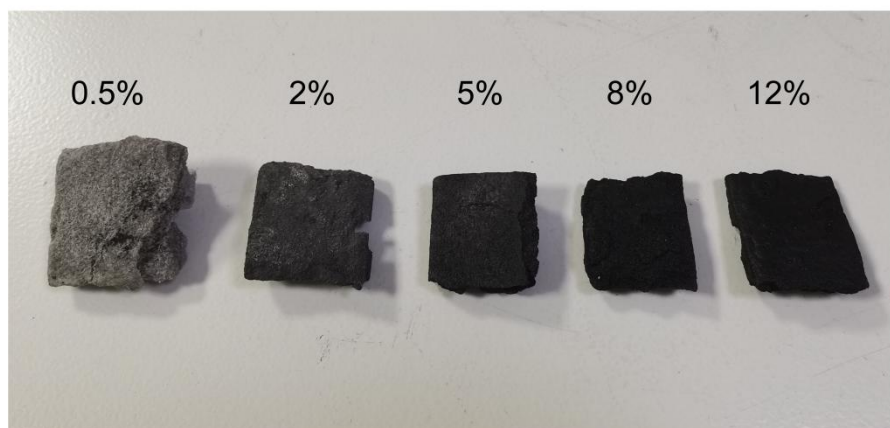
Supplementary Fig. 9. A picture of ICFB sorbent samples with different carbon loadings. Five ICFB sorbent samples are presented, with a carbon loading of 0.5 wt.%, 2 wt.%, 5 wt.%, 8 wt.%, and 12 wt.%, respectively.
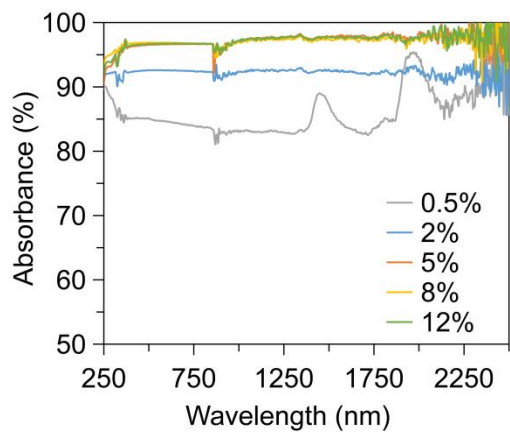
Supplementary Fig. 10. The absorbance of ICFB samples with different carbon loadings. As indicated, the absorbance of the ICFB sample with a carbon loading of 0.5 wt.% under a wavelength of 250~2500 nm is primarily lower than 85%. An increase in the carbon loading contributes to an enhanced solar absorbance of the ICFB sorbent. ICFB samples with a carbon loading above 5 wt.% reach a high solar absorbability of over 95%.
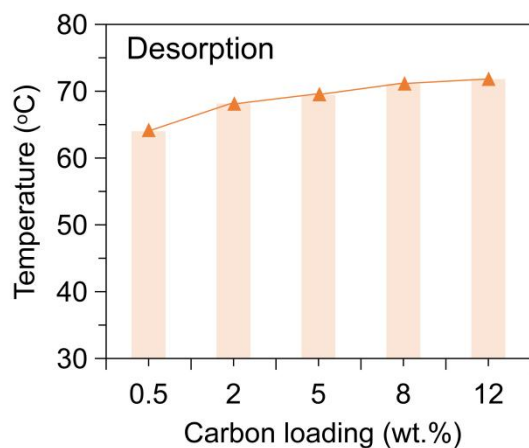
Supplementary Fig. 11. Surface maximum temperature of ICFB samples with different carbon loadings under 1-sun solar intensity. As indicated, with the increase of carbon loading from 0.5 wt.% to 12 wt.%, the surface maximum temperature of the ICFB sample increases.
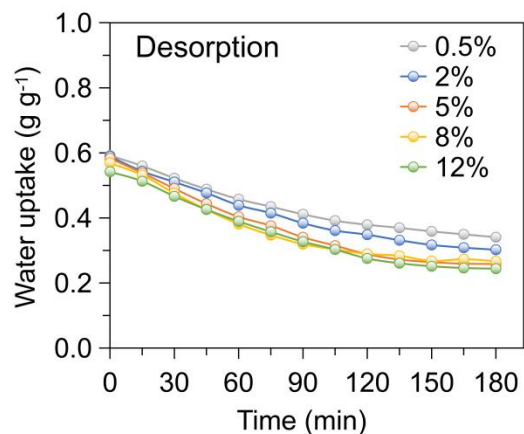
Supplementary Fig. 12. Mass change of ICFB samples with different carbon loadings under 1-sun solar intensity. Compared with the sample with a carbon loading of 0.5 wt.%, the others (2 wt.%, 5 wt.%, 8 wt.%, and 12 wt.%) have faster desorption rate and desorption capacity. However, with the increase of carbon loading from 5 wt.% to 12 wt.%, the desorption performance has subtle change.
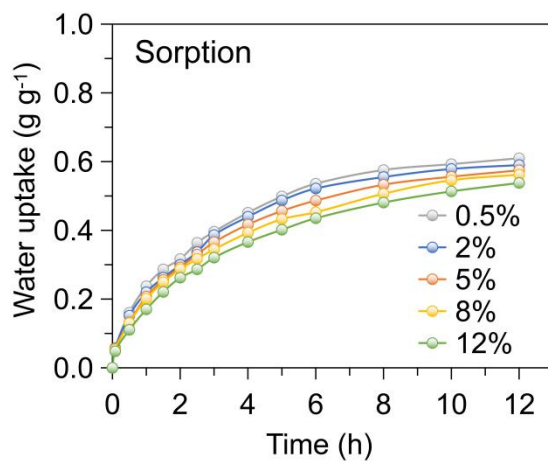
Supplementary Fig. 13. Comparison of water uptake capacity of ICFB samples with different carbon loading. As indicated, with the increase of carbon loading from 0.5 wt.% to 12 wt.%, the water uptake capacity of the ICFB sample increases, with the differences within 10%.

Supplementary Table 1. Comparison of important performances between ICFB and other solar-harvesting matrices.

| Sorbent material	Sorption Capacity (g g⁻¹)	Solar Absorbance (%)	Desorption efficiency (%)	Reference
CaCl2@GO-based aerogel	-	96.2	-	[11]
[Emim][Ac]@carbon fiber membrane	0.65 at 25°C, 60%RH	95.0	62.5	[12]
Steam-80	0.33 at 25°C, 70%RH	96.8	95.5	[13]
ACF-LiCl	1.08 at 25°C, 75%RH	-	-	[14]
ILCA	0.80 at 25°C, 50%RH	95.0	33.0	[9]
ICFB	0.61 at 20°C, 70%RH	95.0	49.8	This work
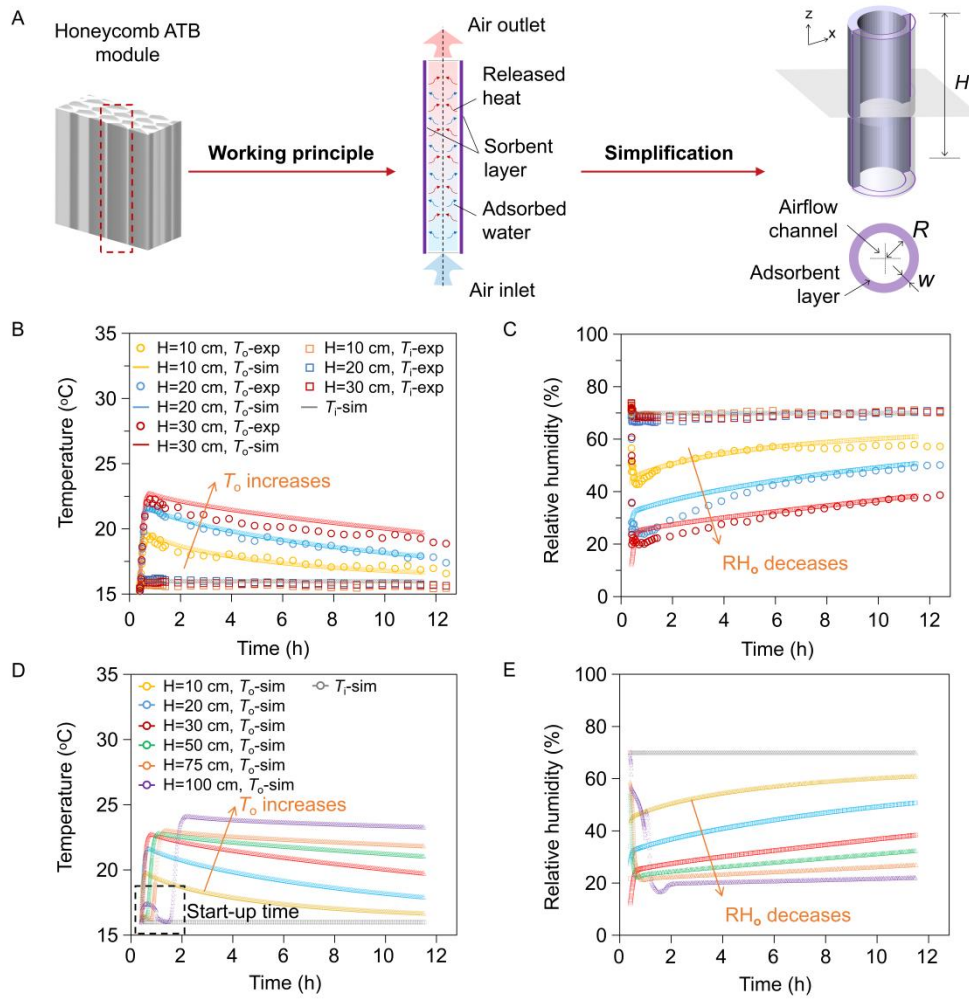
Supplementary Fig. 14. Design and optimization of the honeycomb ATB module: (A) 3D render of the simulation model; (B)(C) verification of the simulation results; (D) (E) the influence of the channel height on the output performance of air. The honeycomb ATB module consists of multiple sets of single channel unit, which is simplified as a cylindrical unit composed of an airflow channel and adsorbent layer. The height and the radius of the airflow channel is defined as H and R, respectively, and the thickness of the adsorbent layer is denoted as w. The results indicate a high degree of coincidence between the experimental and numerical results, which verifies the accuracy of the numerical model. The simulation results show that, with the increase of the channel height from 10cm to 30cm, the output air temperature lift rises from the maximum of 4 °C to 7 °C, and the effective heating duration time extends. For the simulation unit with 100-cm height, the start-up time of effective heating takes as long as 2h, which fails to achieve rapid thermal response. With the increase of the channel height, the dehumidification capacity of the simulation model is also improved, and the outlet humidity is reduced from 40%~60% to 20%~40%. Based on the above analysis, an optimal height of 30 cm is selected based on the above consideration.
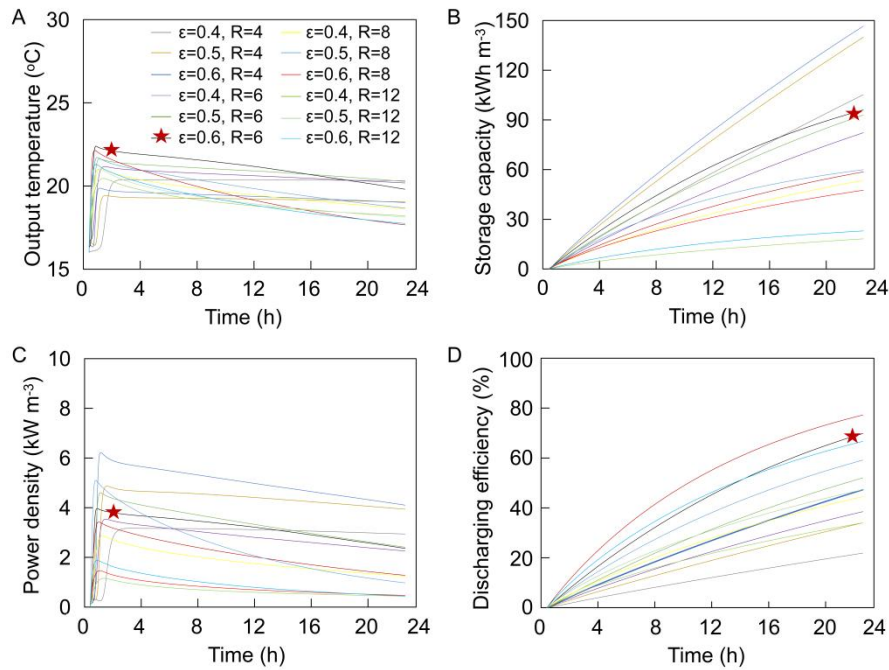
Supplementary Fig. 15. Influence of geometric parameters on the thermal output performance of the simulation model: (A) output temperature; (B) storage capacity; (C) power density; (D) discharging efficiency. The voidage ε is defined as the ratio of the volume of the air channel to the total volume of the simulation unit. The air channel radius and the voidage are shown in the figure. Based on the results, the thermal output performance is optimal when the air channel radius is 6 mm, adsorbent layer thickness is 1.8 mm, and the voidage is 0.6. A maximum thermal storage capacity of 96.0 kWh m^{-3}, an average thermal power density of 3.10 kW m^{-3}, and a discharging efficiency of 69.8%, can be obtained after 22 h of adsorption.
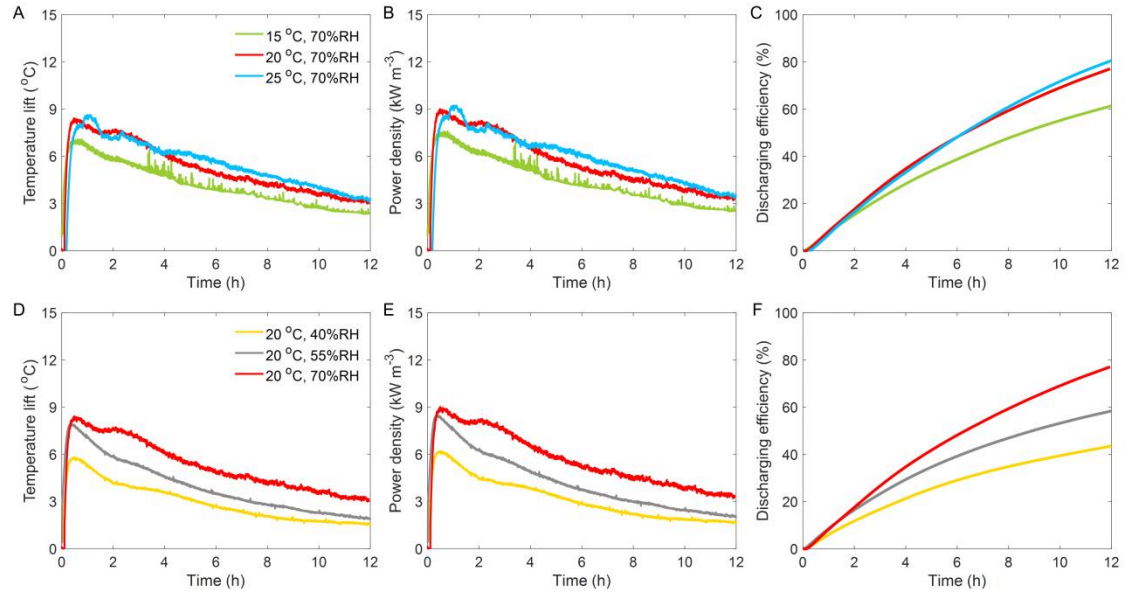
Supplementary Fig. 16. Evaluation of the influences of inlet air temperature and RH on heat discharging performances of ATB the module. The effects of inlet air temperature (15, 20, and 25 °C) on thermal output performances: (A) outlet temperature lift; (B) thermal power density; (C) discharging efficiency. The effects of inlet air RH (40, 55, and 70%RH) on thermal output performances: (D) outlet temperature lift; (E) thermal power density; (F) discharging efficiency. The results indicate that an increase in the inlet air temperature and RH contributes to better thermal output performances of the ATB module.
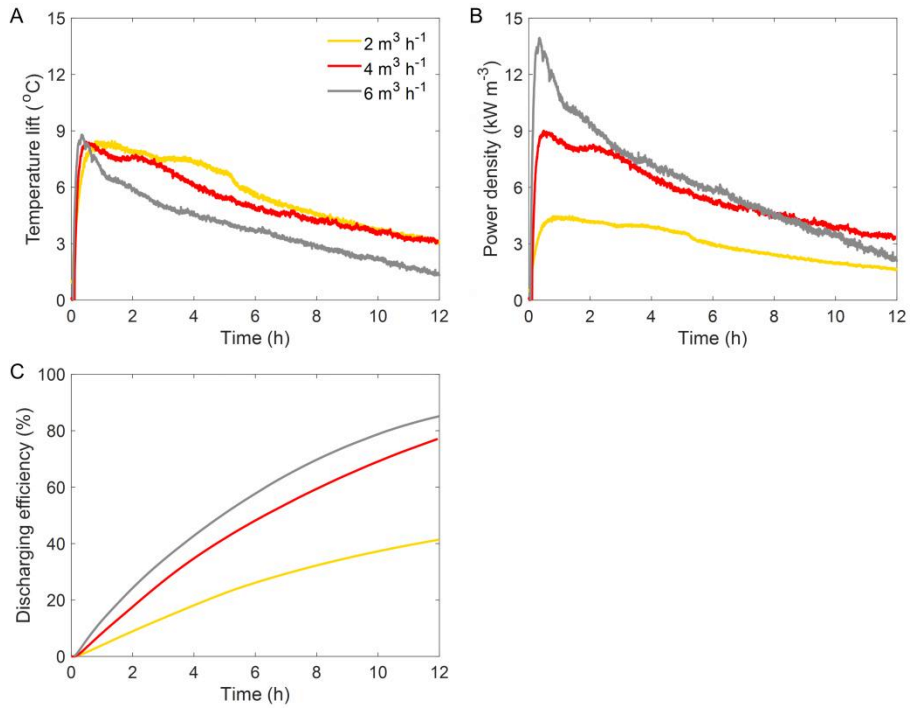
Supplementary Fig. 17. Evaluation of the influences of airflow rate on heat discharging performances of ATB the module. The effects of airflow rate (2, 4, 6 m^3 h^{-1}) on thermal output performances: (A) outlet temperature lift; (B) thermal power density; (C) discharging efficiency. By increasing the airflow rate, an enhancement in thermal power density is achieved as well as discharging efficiency, but the air temperature lift drops. The evolution of the output air temperature and power density is smoother and more stable in the case of low airflow rate.
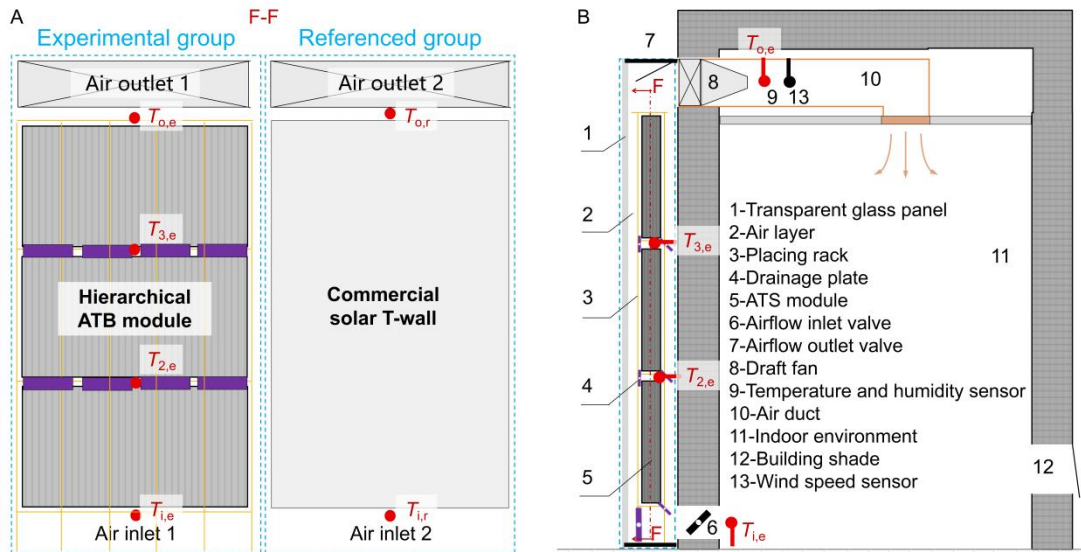
Supplementary Fig. 18. Schematic illustration of the T-wall based ATB apparatus. (A) A sectional drawing of the T-wall based ATB apparatus as an experimental group, and a commercial solar T-wall device as a referenced group in this study. (B) A display drawing of the T-wall based ATB apparatus installed on the building wall for field test. The T-wall based ATB apparatus adopts a hierarchical structure with three ATB modules distributed separately at the upper, middle, and lower positions. The air inlet is at the bottom, and the air outlet is on the top. The distribution of four temperature and RH sensors in the ATB apparatus are denoted as $T_{i,e}$, $T_{2,e}$, $T_{3,e}$, and $T_{o,e}$. Two temperature and RH sensors are applied in the referenced group to measure the inlet air temperature $T_{i,r}$ and outlet air temperature $T_{o,r}$.
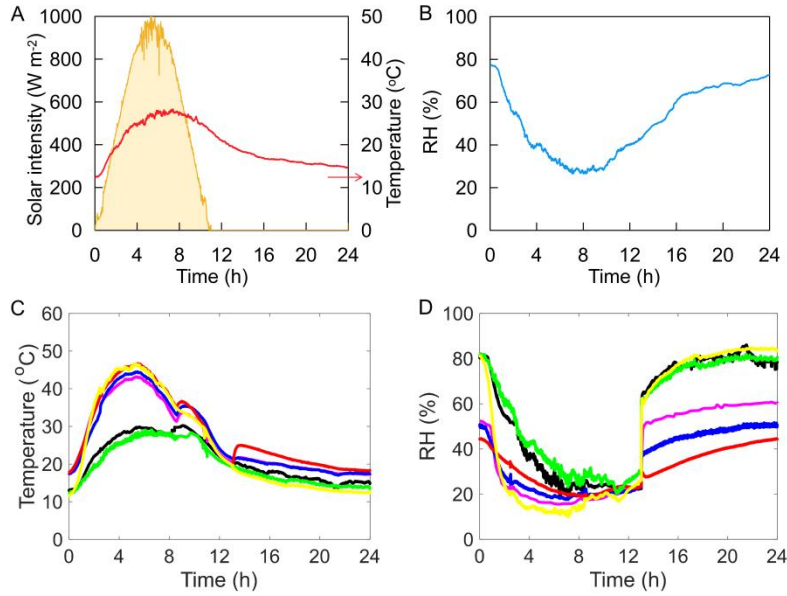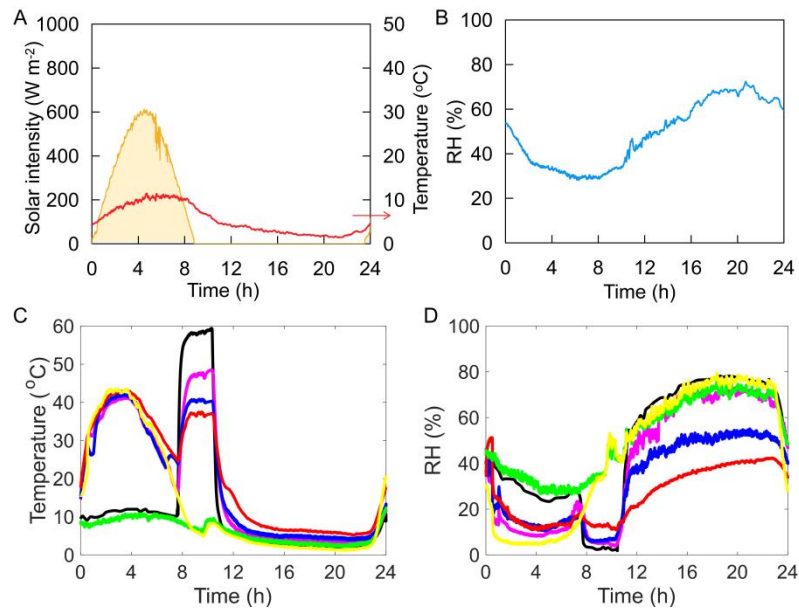
Supplementary Fig. 19. Weather data and thermal performances of Group 1. The testing results of Group 1: (A) the real-time solar intensity and local air temperature variations; (B) the local air RH variations; (C) temperature variations of measurement sites at the ATB apparatus and the referenced T-wall device; (D) RH variations of measurement sites at the ATB apparatus and the referenced T-wall device. The weather in Group 1 represents a typical sunny day with sufficient solar intensity in winter in Shanghai, China. The black, purple, blue and red lines in (C)(D) represent the inlet air temperature of first stage $T_{i,e}$, the inlet air temperature of second stage $T_{2,e}$, the inlet air temperature of third stage $T_{3,e}$, and outlet air temperature $T_{o,e}$ in the experimental group, respectively. The green line and the yellow line in (C)(D) denote the inlet air temperature $T_{i,r}$ and outlet air temperature $T_{o,r}$ in the referenced group.
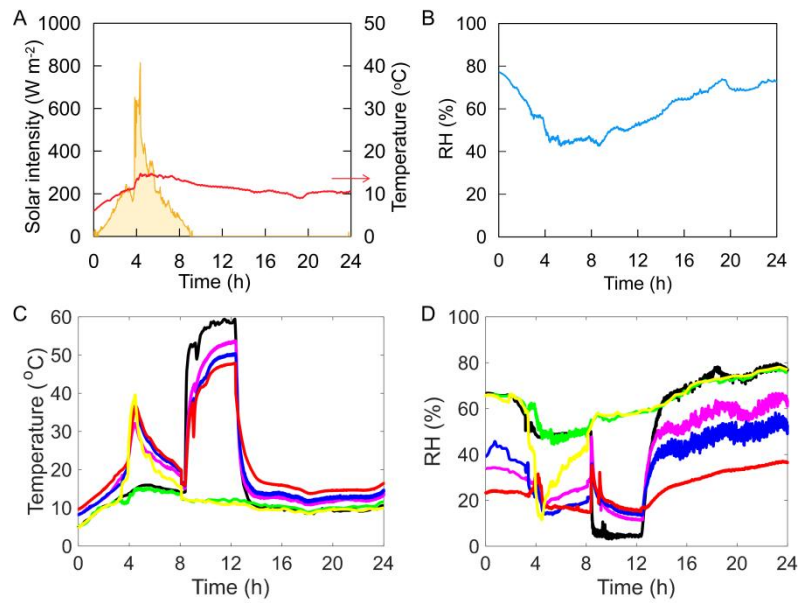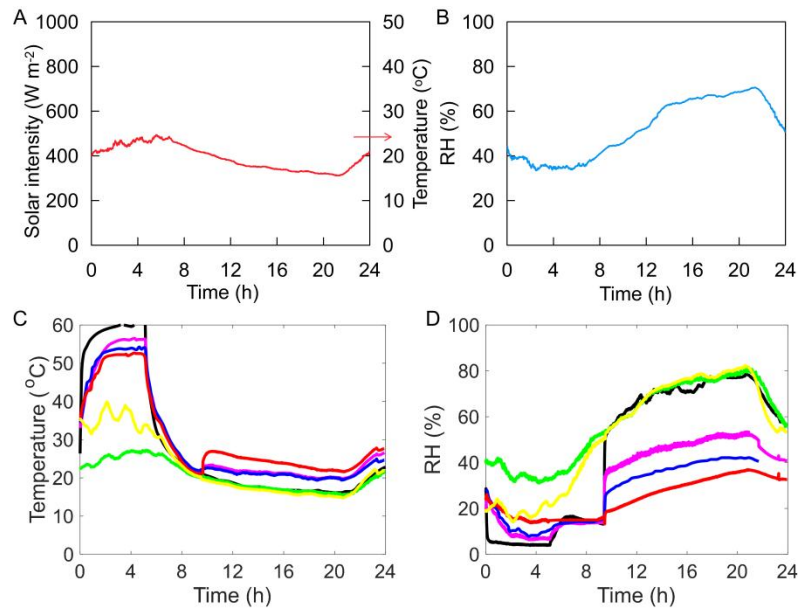
Supplementary Fig. 20. Weather data and thermal performances of Group 2. The testing results of Group 2: (A) the real-time solar intensity and local air temperature variations; (B) the local air RH variations; (C) temperature variations of measurement sites at the ATB apparatus and the referenced T-wall device; (D) RH variations of measurement sites at the ATB apparatus and the referenced T-wall device. The weather in Group 2 represents a typical cloudy day with unstable solar intensity in winter in Shanghai, China.
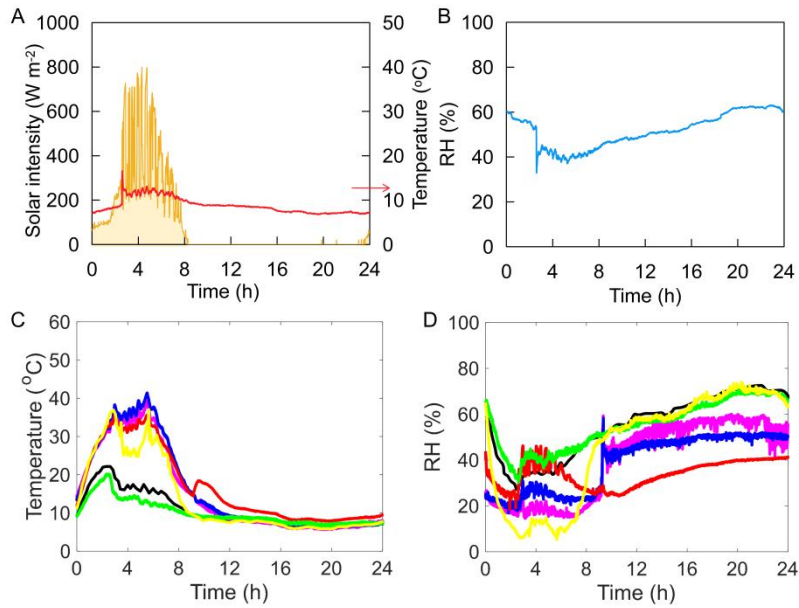
Supplementary Fig. 21. Weather data and thermal performances of Group 3. The testing results of Group 3: (A) the real-time solar intensity and local air temperature variations; (B) the local air RH variations; (C) temperature variations of measurement sites at the ATB apparatus and the referenced T-wall device; (D) RH variations of measurement sites at the ATB apparatus and the referenced T-wall device. The weather in Group 3 represents a typical cloudy day with unstable solar intensity in winter in Shanghai, China.

Supplementary Fig. 22. Weather data and thermal performances of Group 4. The testing results of Group 4: (A) the real-time solar intensity and local air temperature variations; (B) the local air RH variations; (C) temperature variations of measurement sites at the ATB apparatus and the referenced T-wall device; (D) RH variations of measurement sites at the ATB apparatus and the referenced T-wall device. The weather in Group 4 represents a typical cloudy day with insufficient solar intensity in winter in Shanghai, China.

Supplementary Fig. 23. Weather data and thermal performances of Group 5. The testing results of Group 5: (A) the real-time solar intensity and local air temperature variations; (B) the local air RH variations; (C) temperature variations of measurement sites at the ATB apparatus and the referenced T-wall device; (D) RH variations of measurement sites at the ATB apparatus and the referenced T-wall device. The weather in Group 5 represents a typical overcast day with no solar intensity in winter in Shanghai, China.

Supplementary Table 2. Calculation parameters used in the simulation model.

Parameter	Unit	Value
R_{ei}	$m^2\,K\,W^{-1}$	0.239
R_{ee}	$m^2\,K\,W^{-1}$	0.100
g_w	-	0.850
α_{sol}	-	0.950
Q_v	$m^3\,s^{-1}$	0.054
H	m	3
h_c	$W\,m^{-2}\,K^{-1}$	2.50
h_r	$W\,m^{-2}\,K^{-1}$	4.20
$1/h_e$	$m^2\,K\,W^{-1}$	0.043
$1/h_i$	$m^2\,K\,W^{-1}$	0.115
A_w	m^2	18
A_f	m^2	24
$F_S \times F_F \times F_W$	-	0.900
I_w	$kW\,m^{-2}$	0.7 / 0.3
T_i	°C	20
$T_{e,d}$	°C	15
$T_{e,n}$	°C	5
ρ_a	$kg\,m^{-3}$	1.20
$C_{p,a}$	$J\,kg^{-1}\,K^{-1}$	1000
ε	-	1
h_{char}	$kW\,m^{-3}$	6 / 3
h_{disc}	$kW\,m^{-3}$	2 / 1
t_d	h	8
t_n	h	16
h_{diss}	$W\,m^{-2}$	30
ε	-	1

Note: R_{ei}, R_{ee}, h_c, h_r, h_e, and h_i, are intermediate variables in the simulation model. For the detailed information of these variables, please refer to literature [6]. α_{sol}, I_w, T_i, $T_{e,d}$, $T_{e,n}$, h_{char}, h_{disc}, t_d, and t_n are determined according to the experimental data.
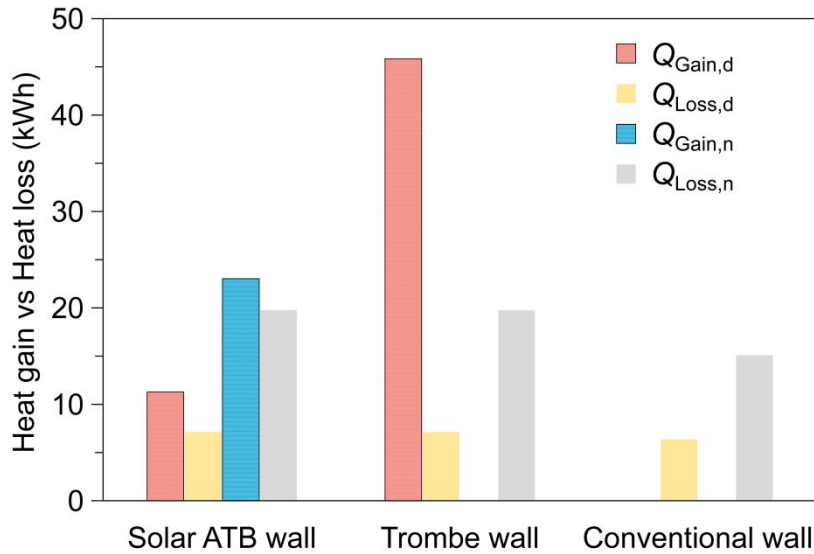
Supplementary Fig. 24. Performance evaluation of energy building systems integrated with different walls, with a high solar radiation intensity of 0.7 kW m^{-2} adopted in the simulation model. $Q_{Gain,d}$ and $Q_{Loss,d}$ represent the heat gain and heat loss in different systems at daytime. $Q_{Gain,n}$ and $Q_{Loss,n}$ represent the heat gain and heat loss in different systems at nighttime, respectively. It is witnessed that, when compared with the conventional wall system, the solar ATB wall and Trombe wall systems possess larger heat loss, which is attributed to the ventilation effect in these two systems. Under a solar radiation intensity of 0.7 kW m^{-2}, both of the building systems adopting solar ATB wall and Trombe wall have larger heat gain against the heat loss during daytime, harvesting solar energy for building heating. However, the heat gain is comparatively smaller in the solar ATB wall integrated building system, due to the heat storage functionality of the solar ATB wall. The stored thermal energy is used to provide a heating effect at nighttime, earning an effective net heating load in the solar ATB wall integrated building system. In the contrast, despite the great heat gain of solar harvesting, the Trombe wall system is unable to satisfy the heating demand at night. In this simulation case, the energy saving of a building using solar ATB wall compared with the conventional wall Q_{ES} is calculated to be 1.605 kWh m^{-2} per day, demonstrating the efficient energy saving effect by employing solar ATB wall in the building envelope.
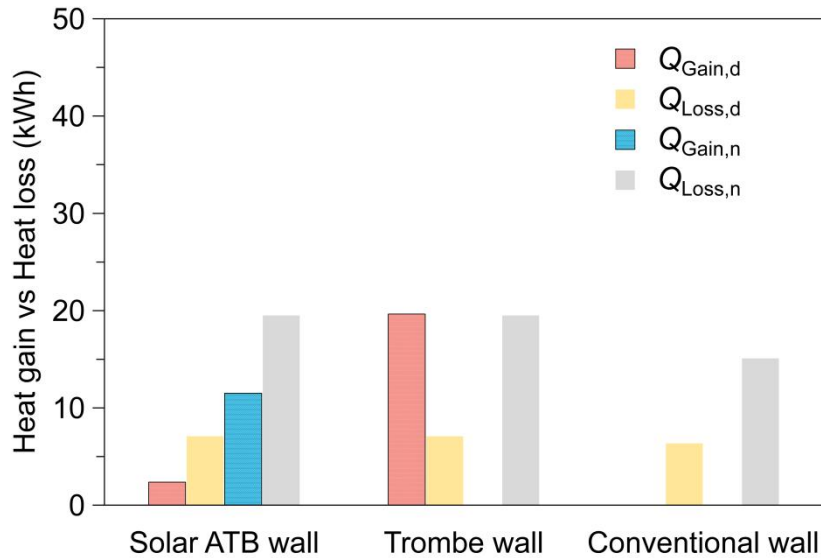
Supplementary Fig. 25. Performance evaluation of energy building systems integrated with different walls, with a low solar radiation intensity of 0.3 kW m^{-2} adopted in the simulation model. $Q_{Gain,d}$ and $Q_{Loss,d}$ represent the heat gain and heat loss in different systems at daytime. $Q_{Gain,n}$ and $Q_{Loss,n}$ represent the heat gain and heat loss in different systems at nighttime, respectively. The heat gains of the building systems adopting solar ATB wall and Trombe wall shrink because of a lower solar radiation in this simulation case. For the solar ATB wall integrated system, the heat gains are smaller than the heat losses at daytime and nighttime, indicating a combination of solar heating and supplementary electric heating is necessary for ATB charging in days with inadequate solar energy, or a need for auxiliary building heating methods. Despite that, even at a low solar radiation intensity of 0.3 kW m^{-2}, the energy saving of a building using solar ATB wall compared with the conventional wall Q_{ES} is calculated to be 0.487 kWh m^{-2} per day. This result suggests that a more substantial study is needed for the integration of solar ATB wall into the whole building systems, contributing to the realization of net-zero energy buildings with highly efficient, grid-interactive and smart-connected strategies.

Reference

[1] X. Li, J. Wen, Review of building energy modeling for control and operation, Renewable and Sustainable Energy Reviews, 37 (2014) 517-537.

[2] J. An, Y. Wu, C. Gui, D. Yan, Chinese prototype building models for simulating the energy performance of the nationwide building stock, Building Simulation, 16(8) (2023) 1559-1582.

[3] Y. Zhang, Z. Zhu, Z. Peng, J. Luo, X. Sun, J. Li, F. Peng, The Trombe wall equipped with PCMs for the enhancement of the indoor thermal quality, Energy and Buildings, 297 (2023) 113407.

[4] P.A. Mathew, L.N. Dunn, M.D. Sohn, A. Mercado, C. Custudio, T. Walter, Big-data for building energy performance: Lessons from assembling a very large national database of building energy use, Applied Energy, 140 (2015) 85-93.

[5] Thermal performance of buildings—calculation of energy use for space heating, UNE-EN ISO 13790, (2004).

[6] Á. Ruiz-Pardo, S.Á. Domínguez, J.A.S. Fernández, Revision of the Trombe wall calculation method proposed by UNE-EN ISO 13790, Energy and Buildings, 42(6) (2010) 763-773.

[7] H. Zhang, H. Shu, A Comprehensive Evaluation on Energy, Economic and Environmental Performance of the Trombe Wall during the Heating Season, Journal of Thermal Science, 28(6) (2019) 1141-1149.

[8] H. Liu, K. Nagano, J. Togawa, A composite material made of mesoporous siliceous shale impregnated with lithium chloride for an open sorption thermal energy storage system, Solar Energy, 111 (2015) 186-200.

[9] F. Deng, C. Wang, C. Xiang, R. Wang, Bioinspired topological design of super hygroscopic complex for cost-effective atmospheric water harvesting, Nano Energy, 90 (2021) 106642.

[10] H. Shan, C. Li, Z. Chen, W. Ying, P. Poredos, Z. Ye, Q. Pan, J. Wang, R. Wang, Exceptional water production yield enabled by batch-processed portable water harvester in semi-arid climate, Nat Commun, 13(1) (2022) 5406.

[11] X. Wang, X. Li, G. Liu, J. Li, X. Hu, N. Xu, W. Zhao, B. Zhu, J. Zhu, An Interfacial Solar Heating Assisted Liquid Sorbent Atmospheric Water Generator, Angew Chem Int Ed Engl, 58(35) (2019) 12054-12058.

[12] H. Qi, T. Wei, W. Zhao, B. Zhu, G. Liu, P. Wang, Z. Lin, X. Wang, X. Li, X. Zhang, J. Zhu, An Interfacial Solar-Driven Atmospheric Water Generator Based on a Liquid Sorbent with Simultaneous Adsorption-Desorption, Adv Mater, 31(43) (2019) e1903378.

[13] Y. Song, N. Xu, G. Liu, H. Qi, W. Zhao, B. Zhu, L. Zhou, J. Zhu, High-yield solar-driven atmospheric water harvesting of metal-organic-framework-derived nanoporous carbon with fast-diffusion water channels, Nat Nanotechnol, 17(8) (2022) 857-863.

[14] J.Y. Wang, R.Z. Wang, Y.D. Tu, L.W. Wang, Universal scalable sorption-based atmosphere water harvesting, Energy, 165 (2018) 387-395.